Impact of laser-induced breakdown spectroscopy implementation for the quantification of carbon content distribution in archaeological ferrous metals

Xueshi Bai, Hortense Allègre, Manon Gosselin, Philippe Dillmann, Maxime Lopez, Florian Téreygeol, Vincent Detalle

Version of Record: https://www.sciencedirect.com/science/article/pii/S0584854720304031
Manuscript_108ef333b8dd1593bca35878d067bcf1

Impact of LIBS implementation for the quantification of carbon content distribution in archaeological ferrous metals

Xueshi Bai[1,2], Hortense Allègre[1], Manon Gosselin[3,4], Philippe Dillmann[4], Maxime Lopez[1,2], Florian Téreygeol[4], Vincent Detalle[1,5,*]

[1]Centre de Recherche et de Restauration des Musées de France (C2RMF), 14 quai François-Mitterrand, 75001 Paris, France
[2]Fondation des sciences du patrimoine/EUR-17-EURE-0021, 33 boulevard du Port, MIR de Neuville, 95011 Cergy-Pontoise cedex, France
[3]CNRS, UMR7041, ArScAn, Equipe GAMA, MAE, Université de Nanterre, France
[4]LAPA-IRAMAT, NIMBE, CEA, CNRS, Université Paris-Saclay, CEA Saclay 91191 Gif-sur-Yvette, France,
[5]PSL Research University, Institut de Recherche Chimie Paris, Chimie ParisTech, CNRS UMR 8247, 75005 Paris, France

[*]**vincent.detalle@culture.gouv.fr**

Abstract

The presence of carbon content is a key enabling factor in archaeological ferrous material studies because it can provide technological and temporal information on its fabrication. A strong relationship exists between the composition, the metallographic structure, and the mechanical properties of metals. Laser-induced breakdown spectroscopy (LIBS) is one of the techniques that can be used in situ to access the carbon content of samples.

The paper presents a thorough investigation of the influence of key experimental parameters on the analytical implementation of LIBS, proposes a suitable protocol for carbon quantification, and discusses its limitations. We demonstrate that the global carbon concentration can be obtained with the help of a large laser spot, but this is not sufficient to separate all steel phases. To overcome this problem of spatial distribution and to achieve quantitative measurements, a smaller laser spot has been used and a specific analytical procedure has been developed. As a result, a smaller spot is needed for detecting the different steel phases and to show the metallographic structure. On a macro-scale, a preliminary sampling can be performed with a larger laser spot on the objects in situ in order to locate the high carbon content, such as cementite (Fe_3C), for further analysis. On a micro-scale, the

different phases of steel and their distribution in the object should be precisely and locally determined with a smaller laser spot, even on nonequilibrium structures. This opens up prospects for researchers to quantify the presence of different phases within the steel matrix and correlate such findings with the technological background behind steel making in historical times.

Key words: Laser-induced breakdown spectroscopy (LIBS) implementation, Quantitative analysis, Archaeological ferrous metals, Carbon content, Steel phase characterization

1. Introduction

Archaeometallurgy is an interdisciplinary science that consists of studying ancient metallurgical artefacts (their nature, dating, provenance…) in order to answer questions linked to the evolution of ancient production processes, technical know-how, and circulation of materials. One of the key questions in the history of technology is to determine the perception of the nature of the metal (quality) in ancient societies, which is linked to its technological, economical, or cultural values. In fact, a strong relationship exists between the composition, the structure, and the mechanical properties of metals [1]. Among other parameters, carbon content is one of the most influential on the mechanical behavior of iron and steel. For example, the hardness of an iron containing 0.8 wt% carbon is two times higher than one with 0.2 wt% carbon [2]. Determining the carbon concentration is key for any archaeometallurgical study.

The carbon distribution inside archaeological alloys is very heterogeneous [3] compared to modern alloys due to the peculiarity of ancient ironmaking processes taking place at relatively low temperatures compared to contemporary processes [4]. In a given artefact, the carbon content can vary from <0.02 wt% (ferrite) to 0.8 wt% (eutectoid steels). The zones with different carbon content can be separated by tens of micrometers [5]. Thus, in order to understand the nature of the materials of archaeological artefacts, a technique with a good spatial resolution is necessary. Nano-beam secondary ion mass spectroscopy (SIMS) is now used for assessing elemental distribution in steels and mapping of metallographic phases[6]. It is capable of reaching a sub-micrometer spatial resolution. However, it is limited to atomic-scale investigation and is difficult to apply to a big surface; it is especially difficult to use it to perform an in situ measurement under ambient atmosphere.

To obtain the C content distribution of archaeological artefacts quantitatively, the most employed procedure currently is based on a classical metallographic approach using samples taken from the artefacts [5]. Polished sections sampled on artefacts are etched by a Nital solution (4%wt of nitric acid in ethanol) which reveals the metallographic structure (grain boundaries and phases such as ferrite, pearlite--a mix of cementite (Fe_3C) and ferrite, cementite, etc.)[7]. The carbon content can be deduced locally from the proportions of these different phases and the use of a binary Fe-C phase diagram. This quantitative metallographic analysis based on thermodynamic considerations is only reliable at equilibrium state and presents other important limitations. The cooling of the Fe-C alloys was often not slow enough and far from the equilibrium conditions. Consequently, different kinds of structure can appear (Widmanstätten structures, bainite, and martensite if the metal is quenched) that at least generate an error for the C content determination and sometimes makes the approach impossible. Moreover, this method is laborious, time-consuming, and very cumbersome to implement for in-situ observations. In addition, it lacks spatial precision for some non-equilibrium structures. Therefore, the implementation of other quantitative methods based on physicochemical approaches allowing a good spatial resolution (tens of micrometers) is required.

In this case, Laser-Induced Breakdown Spectroscopy (LIBS) could provide an easy way to solve problems of in situ analysis by its advantages as a fast-non-contact technique and with a potential for on-site measurements for all elements in the periodic table. LIBS requires no sampling and avoids chemical contamination from the instrument, and its use can be extended to both polluted surfaces and liquids [8-10]. It has been proved to be a suitable method for the detection of carbon; even when carbon is present in small quantities as in the case of ferrous alloys in industrial applications [11, 12].

Moreover, many recent studies have focused on the development of LIBS for analysis of the carbon content in steel [11-14]. However, considering the heterogeneity in archaeological alloys, the results can differ according to laser spot sizes and analyzed surfaces or volumes [15]. LIBS has been carried out in macro analysis and the spatially resolved (micro) analysis with limits of detection as low as 10 µg/g (~0.001 wt%), which makes the use of this technique to analyze archaeological ferrous metals promising [16-19].

Nevertheless, in these works, the examined carbon emission lines are usually at 193.09 nm or 247.86 nm. They are in the far UV or UV-visible spectral range, which requires a spectrometer sensitive enough for this range. Moreover, in the same spectral range, the iron

from the steel matrix has a very large number of emission lines, which may induce a strong interference with the carbon line and generate a difficulty in observing the carbon emission signal. This work thus focuses on the LIBS implementation in order to establish a protocol for characterizing archaeological artefacts by carbon content quantitative analysis. Carbon content calibration is carried out for two different laser spot sizes, in a so-called macro- and micro-analysis, respectively. This study achieves faster and more stable quantitative analyses and improves the efficiency in the estimation of carbon content in archaeological ferrous metals.

2. Metallographic structure of reference samples and examined archaeological piece

2.1. Reference samples

In order to cover the full range of carbon concentration levels in archaeological ferrous metals, six reference steel samples were used to build a calibration curve for quantitative analysis. Their carbon concentrations, shown in Table 1, were measured beforehand by combustion infrared absorption by Bureau Veritas, Metallurgy Laboratory.

Table 1 The carbon concentrations of the standard samples acquired by combustion infrared absorption

No. Reference sample	Concentration of Carbon (%wt)	Uncertainty (±%)
1	0.006	0.001
2	0.08	0.009
3	0.44	0.05
4	0.45	0.05
5	0.59	0.06
6	0.75	0.08

These six samples were all fixed in the same resin block, and the analyzed surfaces were on the same side. This system may have helped to keep the same experimental conditions when we changed the samples. Figure 1 from No.1 to No.6 shows the microstructural observation by optical microscopy of the reference samples after Nital etching. The structure corresponds to ferrite-pearlitic steels tempered and cooled slowly. Pearlite (carbon: 0.8%wt) appears in dark on the micrograph, and ferrite (carbon: <0.02 wt %) appears in white. The magnification

was not sufficient to solve the pearlite and reveal the ferrite/cementite lamellae. The distribution of different phases was homogenous in the sample, and grains were equiaxed. Conversely, on a scale inferior to several tens of micrometers, the surface became heterogeneous because of the different sizes of the grains (10 – 100 µm).

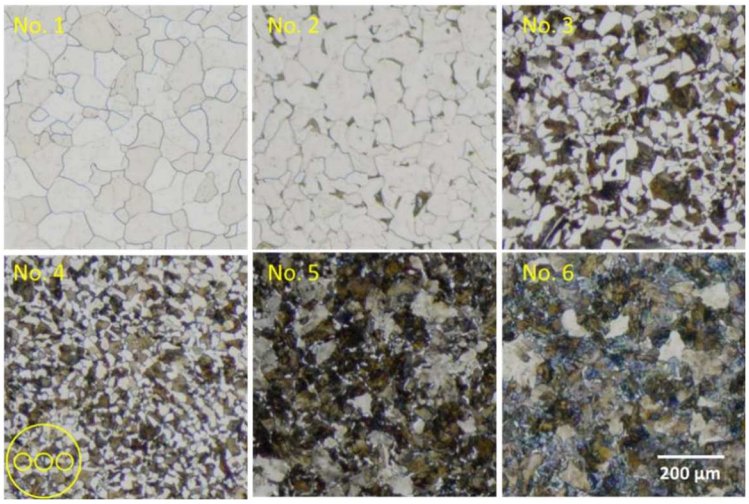

Figure 1 No.1-6: the microstructural observation by means of optical microscopy of the reference samples after Nital etching of the reference samples. Diagram for the interaction zone with different diameters of laser beams (circles on No. 4).

Different spatial measurement resolutions enable us to obtain different kinds of results according to the size of the laser spot compared to the grain size of the steel structure (here about several tens of micrometers). The different diameters of laser beams mark the interaction zone shown as circles in Figure 1 No. 4. A significantly larger spot than this grain size allows us to catch an average composition while a smaller laser spot, with a size comparable to the one of the steel grains, has an ability to reveal the different steel phases within the metallographic structure (micro-analysis/mapping). This shows that LIBS enables new ways of characterization of archaeological ferrous metals.

2.2.Archaeological sample

We selected an archaeological artefact from the Castel-Minier site in Ariège, France [20, 21] in order to showcase the performance of our approach with respect to archaeological samples. The artefact is a plate fragment being forged. This artefact is dated from a period between the end of the 13th century and the beginning of the 14th century. The piece is shown in Figure 2 after cutting and sampling, and the analysis was performed on its cross section.

Figure 2 Archaeologic sample (CL13286) after being cut, and its cross section.

The optical microscopic observations of the polished (grade 80 to 4000 and diamond paste 3 and 1 µm) cross section before and after Nital etching are shown in Figure 3 a) and b). A carbon content distribution map was deduced using optical microscopy and is shown in Figure 3 c). Different ranges of carbon content are distinguished locally according to the visual proportions of each phase (pearlite and ferrite), which can be compared to the standard Fe-C phase diagram [3, 5]. The carbon concentration varies from below 0.1 wt% to above 0.7 wt%. We examined the carbon concentration on this sample with LIBS using the calibration curve from the reference samples.

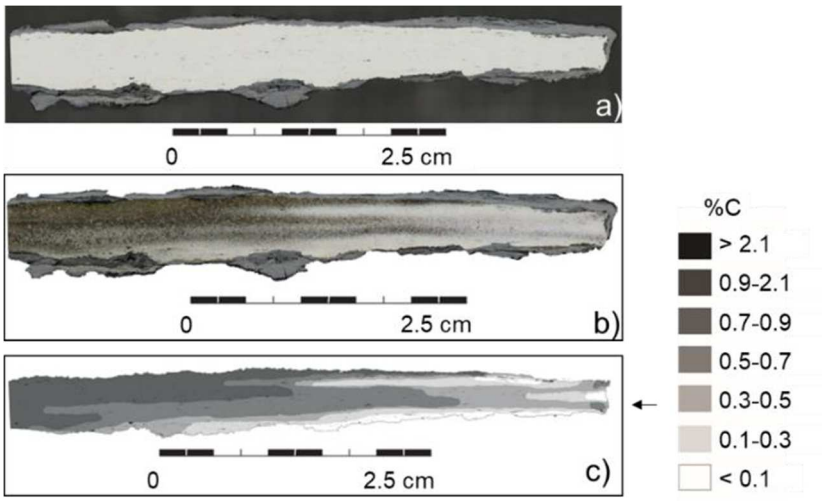

Figure 3 The optical microscopic images before (**a**) and after (**b**) Nital etching of the cross section of the archaeologic sample; **c**) the obtained carbon content distribution.

Optical mapping provides spatial details to determine the carbon distribution by observation. LIBS analysis measures both carbon distribution and carbon concentration for each position.

3. Experimental setups and analytical strategy

3.1. Experimental setups and measurement protocols

In order to address this issue, we adjusted our experimental setups to perform carbon calibration and LIBS mapping. The experimental setup is presented in Figure 4. A Nd:YAG laser (laser: ULTRA, Lumibird Quantel, France) provides the fundamental emission of Nd:YAG laser at 1064 nm with a nominal pulse duration of 8 ns (FWHM), operated at 20 Hz. The pulse energy delivered on the sample surface was adjusted and controlled by an attenuator and a power meter. A mechanical beam shutter controlled the number of laser shots delivered on the sample surface. Two different lenses with a focal length of 300 and 75 mm were used to focus the laser beam onto the sample surface in order to obtain different laser spots corresponding to macro- and micro-analysis, respectively. The sample surface was placed on the focal plan of each lens. The laser pulse energy was adjusted for the purposes of keeping the same laser fluence at 33.2 J/cm^2 for these two ablation configurations.

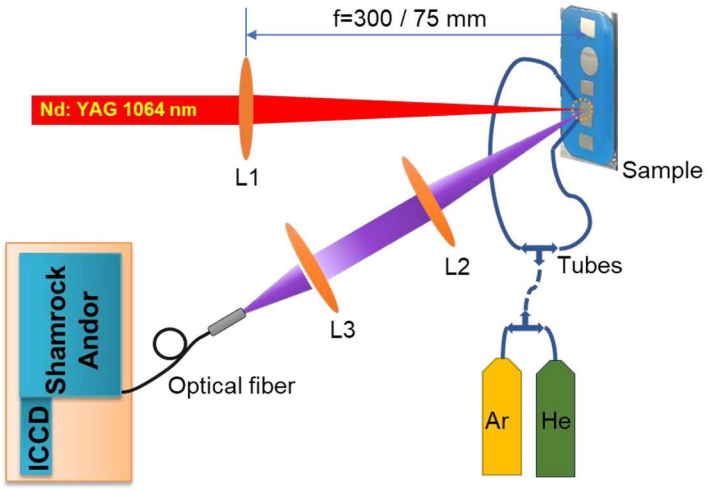

Figure 4 Experimental setup. L1-3: Fused silica plano-convex lens.

The plasma emission was collected by a lens (L2: f=15 cm) and transmitted through a fused silica optical fiber (UV/VIS, IDIL Fibres optiques, France) placed in the image plane of the 4f imaging system with L2 and L3 (f=10 cm). The fiber was connected to a Czerny-Turner spectrometer (Shamrock 303i, Andor Technology, UK) with three gratings of 600, 1200, and 1800 lines/mm and was coupled to an ICCD camera (DH340T-18F-E3, Andor Technology, UK). Time-resolved detection was performed for spectroscopic measurement by triggering the ICCD camera with the synchronization signal generated by a delay generator. Each spectrum was acquired on a single-shot basis, and a series of 250 spectra were recorded from the same crater on the sample for one measurement. Due to a large number of iron emission lines, it

was necessary to use a grating with good resolution [22]. Therefore, a 1800 lines/mm grating was used, but it was still difficult to eliminate the interference with the iron lines for C I 247.86 nm. As a result, the carbon emission line at 193.09 nm (C I) is used in this work to examine the carbon content. This carbon line has a high emission efficiency (Transition probability: $A_{ki}=3.39\times10^{8}$ s^{-1}), which may compensate a portion of the intensity lost from the strong far-UV spectral absorption by the air. In addition, the chosen grating was optimized for the 200 nm spectral zone, so that the high sensitivity allowed the observation of this line even from the low carbon concentration sample. The detection windows are shown in Table 2. The delay described the time interval between the beginning of detection and the laser pulse arriving at the surface, and the gate is the duration of detection of the ICCD camera.

A controlled environment surrounding the laser impact zone was created by a pair of gas blowing tubes (4-mm diameter) installed above the target in order to neutralize the influence of carbon emission from ambient air. The adjusted flow ensured the expansion of the plasma into an environment at atmospheric pressure, effectively removing the contribution of air. Two types of noble gas were used—Argon and Helium. The gases were mixed into the same tube by a "T-connecter". The gas mixture propagated in a long tube of about 8 m length between each bottle before being separated into two tubes. This distance allowed the two gases to be mixed homogeneously. The plasma emission was directly conditioned by temperature and electron density. As shown in the literature[23, 24], the higher temperatures and electron densities are obtained in argon, and the lower ones are found in helium. In order to get the best signal to background ratio from the emission, the flux proportion of each element in the gas mixture was optimized for each analysis as shown in Table 2.

Table 2 Parameters for macro-analysis with a 300 mm focal lens and micro-analysis with a 75 mm focal lens

Focal length of lens (L1) (mm)	**Laser spot diameter (µm)**	**ICCD parameters**		**Environment**	
		Delay (ns)	Gate (ns)	Ar (L/min)	He (L/min)
300	220	1200	1200	0.5	3
75	50	400	1500	2.5	0.5

Figure 5 shows the typical spectra from sample No. 1 and 5 averaged from 250 spectra for each sample from macro-analysis configuration. The two spectra are normalized by the

intensity of the Fe II line at 204.06 nm to highlight that the iron (matrix) emission is identical, but not the carbon emission intensity due to its different concentration.

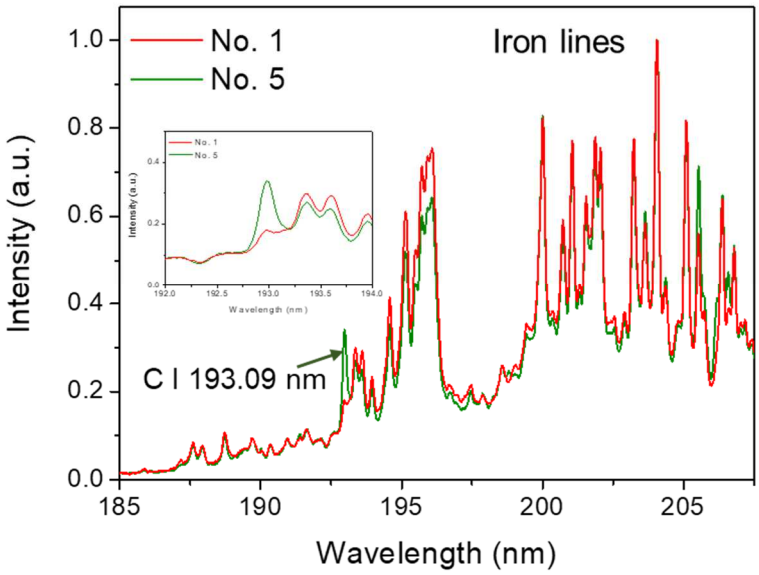

Figure 5 Macro-analysis spectra from sample No. 1 and No. 5.

The grating chosen has a sufficient spectral resolution, which allows us to separate and extract the carbon emission line intensity without interference from the iron lines and furthermore to obtain a calibration with good precision (inset in Figure 5).

3.2.Evaluation and validation of laser ablation

The quantity of matter for analysis is a key determinant of the precision of a quantitative analysis. Assessing ablations is therefore necessary to measure the ability of LIBS analysis in these configurations.

3.2.1. Impacted volume by macro LIBS analysis

Figure 6a and b show images from the optical microscopy of sample No. 5 after 2 and 250 laser shots, respectively. After two laser shots at the chosen fluence on the surface, no measurable crater was present. The affected surface areas remained the same. This enabled us to perform depth measurements without increasing the impacted surface. The microscopic 3D images of the same crater after 250 shots is shown in Figure 6c, where the height is shown using false colors. In Figure 6d, one profile of the crater is plotted at its central position (dotted line in Figure 6c), and the crater depth is estimated at about 17 µm. As a result, the penetration depth for one shot is about 68 nm, which is the depth resolution for this macro-analysis configuration. Considering the conic form of the crater, the volume is estimated to be

about 2.154×10^{-7} cm^3 for 250 laser shot measurements, which is 8.62×10^{-10} cm^3 for one shot ablation.

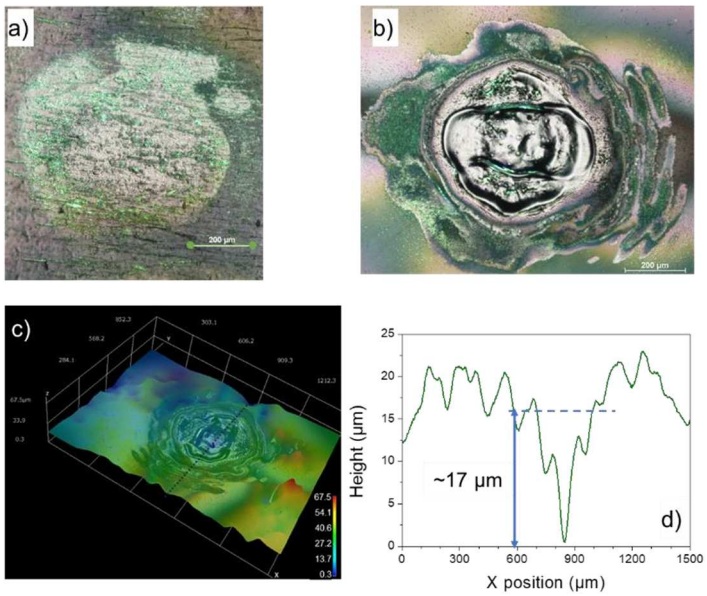

Figure 6 From the sample No. 5 with laser beam of macro analysis: Image from the optical microscopy after 2 (**a**) and after 250 (**b**) laser shots; **c**) microscopic 3D image and **d**) the profile of the center of the crater after 250 shots.

3.2.2. Impacted sample volume by micro LIBS analysis

Micro-analysis was carried out by a series of 9 positions on the surface with a distance of 100 µm between each position in order to provide a fresh surface to the new crater. The measuring path for the six reference samples is the same and is shown in Figure 7a. It is therefore possible to follow their path to look for the various spatial distributions for each sample according to their different plasma emissions.

The microscopic 3D images of the same crater after 250 shots are shown with "real color" (Figure 7b) by using a polarizer in order to remove the specular reflection, and with false colors (Figure 7c) that present different heights on the sample surface. One profile of the craters (Figure 7d) is plotted at central position X(1-3)Y2 (the dotted line in Figure 7c), and the mean value of the crater depth is estimated to be about 36.7 µm. As a result, the depth of measurement for one shot is about 0.15 µm, which can be described as the depth resolution for this micro-analysis configuration. Considering the conic form of the crater, the volume of one crater is estimated to be about 2.402×10^{-8} cm^3 for 250 measurements, which is 9.608×10^{-10} cm^3 for a one-shot ablation.

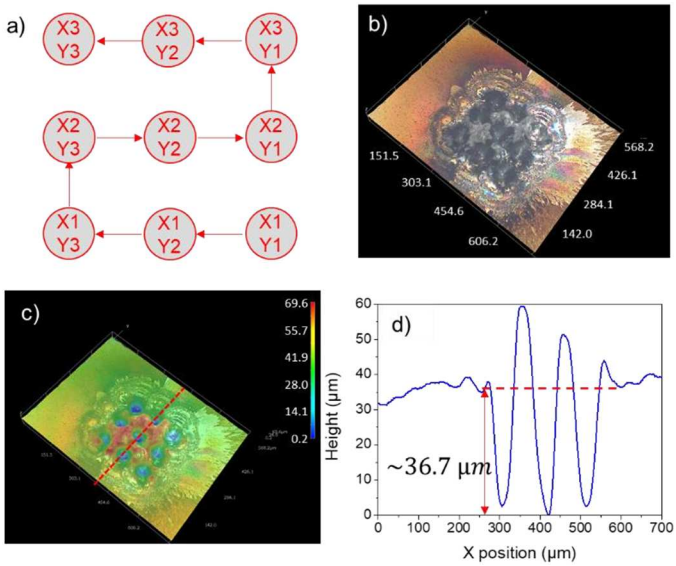

Figure 7 a) Measuring path of micro-analysis. On sample No. 5: Microscopic3D images of the same crater after 250 shots on "real color" (**b**), on false colors (**c**), and profile of craters (**d**).

The total volume analyzed of these 9 craters is about 2.162×10^{-7} cm^3 and is equivalent to that of one macro-analysis crater. Finally, in order to compare these two approaches, we analyzed the same quantity of material using these two different spatial resolution measurements.

4. Results and discussions

In our previous study [25], we demonstrated that an internal standard method [26, 27] is necessary to have a better result for quantitative analysis. The upper transition energy levels for these two lines are close to 7.685 eV for C I and 8.038 eV for the Fe II line (204.06 nm). The iron first ionization energy is 7.902 eV [28]. Therefore, we need a similar electron energy to excite both carbon atoms and iron ions. Moreover, iron is the abundant element. Its content can be considered to be constant for all analyzed samples, including reference samples and archaeological samples, as long as sufficient resolution is maintained; Fe II 204.06 nm was therefore used as the normalized reference line in this work, and the intensity ratio between C I 193.09 nm and Fe II 204.06 nm was used to establish the calibration curve and to perform the analysis on the archaeological sample.

4.1. Macro-analysis on reference samples

Metal cross-sections were polished with a medium containing carbon (diamond paste). This procedure generates surface pollution. Hence, a process to remove the contaminated layer should be implemented to determine the real carbon content.

4.1.1. Intensity distribution as function of depth

In order to evaluate the impact of the polluted surface and the signal evolution, we examined the experimental spectra intensity as a function of depth to evaluate the number of laser shots necessary to get the global concentration. Every ten spectra in depth were averaged, and we extracted the intensity of the C I and Fe II lines for 6 reference samples. The emission intensity of the carbon and iron lines (shown in Figure 8) is divided by the maximum value among all samples and all depth positions and presented as percentage. In Figure 8a, the carbon intensity presented a similar maximum value of all samples for the first ten laser shots close to the surface (about 0.68 µm), which may be due to surface pollution. The carbon line intensity still dropped between the twentieth and thirtieth laser shots with a 20% difference. After that, the intensities seem to be stable, and the variance is less than 10% for most cases. In Figure 8b, the intensities of the Fe II line remain in a small variation range of less than 10%, which means that the plasma was in the same state. The fluctuation of the Fe II line may come from the variance of laser pulse-to-pulse stability.

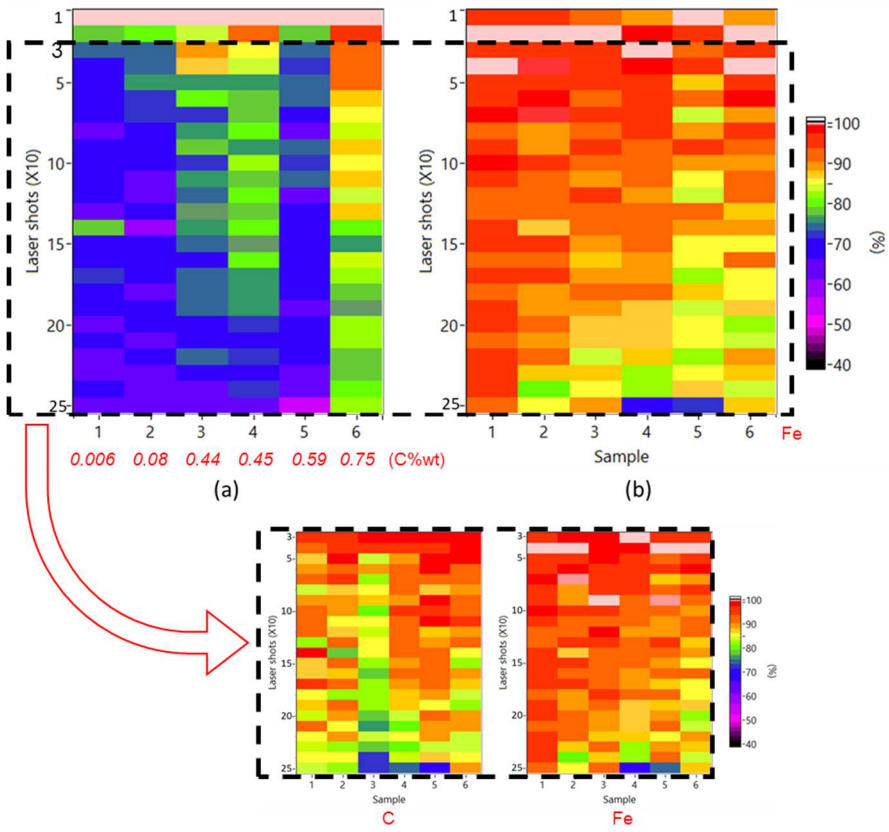

Figure 8 The intensity of C I (**a**) and Fe II (**b**) of every 10 averaged spectra as function of depth for standard samples from macro analysis. The intensity after removing the first twenty first laser shots is in the sub-figure.

The superabundant carbon content on the surface is not representative of the sample, so the spectra from the first twenty laser shots, which correspond to about 1.36 µm, will not be taken

into consideration. As shown in the inset of Figure 8, the intensity from carbon and iron becomes more homogeneous as a function of depth (number of laser shots). However, despite the elimination of the surface contamination, the inhomogeneous carbon intensity for each sample in depth is still present. This may be due to the analysis depth (~0.68 µm) for each of the ten shots, which is inferior to the grain size of tens of micrometers as the surface image shows. This means that the carbon distribution in depth is also inhomogeneous. The remaining 230 "clean" spectra were therefore used to build the calibration curve after being averaged (as mentioned in our experimental condition for 250 laser shots) in order to reduce this depth effect.

4.1.2. Calibration curve for macro quantitative analysis

The intensity ratio of C I 193.09 nm to Fe II 204.06 nm is presented in Figure 9 after averaging 230 spectra for each sample. We plotted these intensity ratios as a function of carbon concentration in Figure 9; the fitted curve has a coefficient of determination (R^2) of 0.9956, and its 95% confidence band is shown between two blue dotted lines. The calibration curve shows a good figure-of-merit for quantitative analysis.

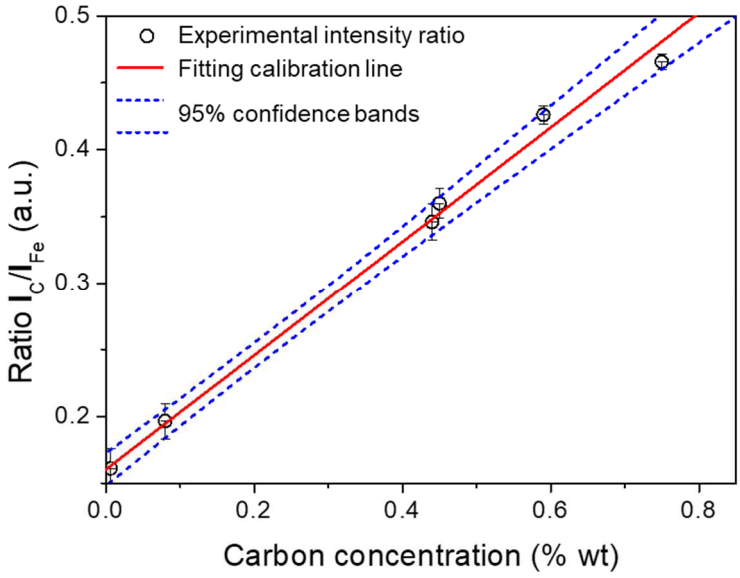

Figure 9 Macro analysis calibration curve from the intensity ratio of carbon and iron line of 230 averaged spectra.

As discussed in the previous section, minimizing analytical volume is necessary and should be optimized. Thus, we have to assess the number of laser shots or spectra that are necessary to obtain a representative result. The value of R^2 can reflect the figure-of-merit for quantitative analysis: the more the value of R^2 is close to 1, the better the linear fitting for the calibration.

The procedure to achieve usable calibration with a minimally destructive volume was set by calculating the coefficients of determination for each possible calibration curve.

We removed from our selection a certain number of spectra from the surface, with which we can select the depth to start the analysis. This is shown in Figure 10a. We then extracted the intensity of the C I and Fe II lines to calculate their ratio. We built the calibration curve from these selected spectra. In the last step, the ratio was plotted as a function of carbon concentration, which gave us the coefficient of determination (R^2) from the linear regression.

The coefficients of determination for all these attempted calibration curves are shown in Figure 10b. We can conclude from this figure that the influence of the surface pollution can be reduced if we accumulate a sufficient number of laser shots. As a principle, the more spectra used to build the calibration curve, the better the linear fitting. However, minimizing the analyzed material and the duration of analysis are crucial. It leads to a compromise between the accuracy of the analysis and limiting the material sampling and the time spent. Figure 10b demonstrates that R^2 values become high enough from averaging 50 spectra after deleting the first twenty spectra that came from the pollution layer.

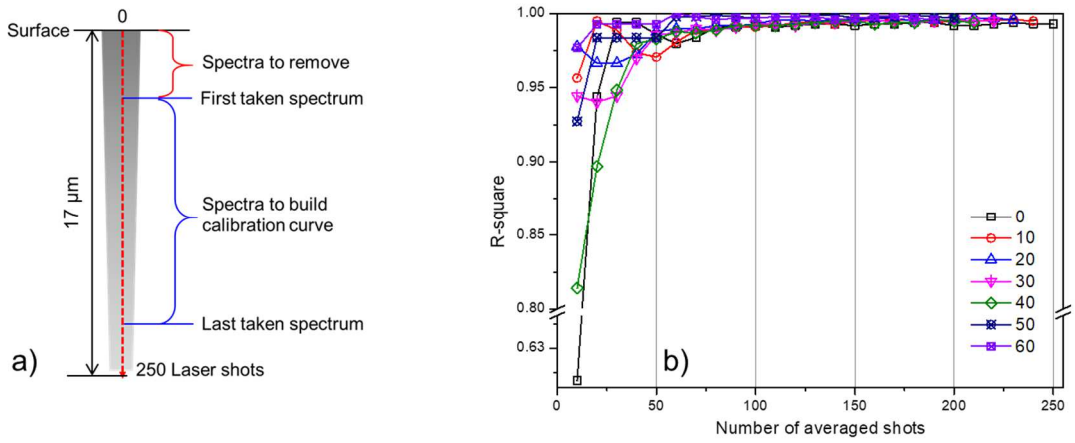

Figure 10 a) Diagram of spectra selection; **b**) Coefficients of determination (R^2) for all attempts of macro-analysis calibration curves after deleting the indicated number (0-60) of spectra from the surface.

As a result, considering the above-mentioned factors, we discarded the spectra from the first 20 laser shots and averaged the following 50 spectra to build the final calibration curve, shown in Figure 11. The R^2 is 0.9871. Although the R^2 decreases, the analyzed volume is reduced by a factor of more than 3 times with only 70 laser shots instead of 250. When using a 20 Hz laser, the required analysis time is about 3.5 seconds per sample. It is therefore possible to perform the analysis on a large number of samples by optimizing its duration, which is useful when studying an extensive corpus of samples.

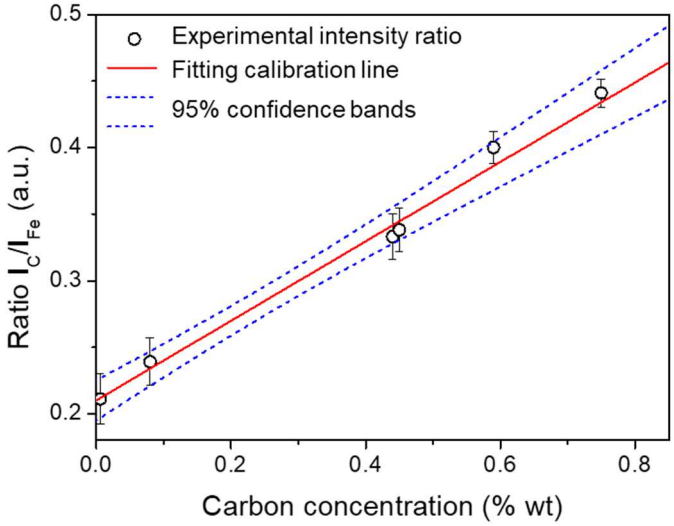

Figure 11 Macro-analysis calibration curve from the intensity ratio of carbon and iron line by averaging 50 spectra after discarding 20 laser shots.

4.2. Influence of the laser beam diameter

As shown in Figure 1, inhomogeneities may appear when the diameter of the laser beam used for analysis becomes smaller and because carbon is mainly present in the 10 µm pearlite grains (at a level of 0.8%wt carbon).

4.2.1. Examination of carbon spatial distribution on the surface

The 250 spectra for every crater were averaged to only reflect the influence of the surface distribution. The ratios of C I 193.09 nm and Fe II 204.06 nm were extracted for 9 analyzed points separately for each sample. We then plotted the ratio from the same position as a function of carbon content which can be seen in Figure 12. Two series of the same experiment were performed—one (black points in Figure 12) was done at the same time as the macro-analysis, and the other (red points) was carried out six months later. The same tendency in these two series indicates the same structure for each sample. As modern alloys, they are homogeneous at macro scale but not at micro-scale. The micro-analysis with a small laser spot can thus perform a phase distribution detection, but it cannot be used to build the calibration curve. As one position can no longer represent the given global carbon content from the combustion, an average method without the spatial resolution is required. We therefore adapted our methodology in order to overcome this inhomogeneity and get a relevant calibration curve.

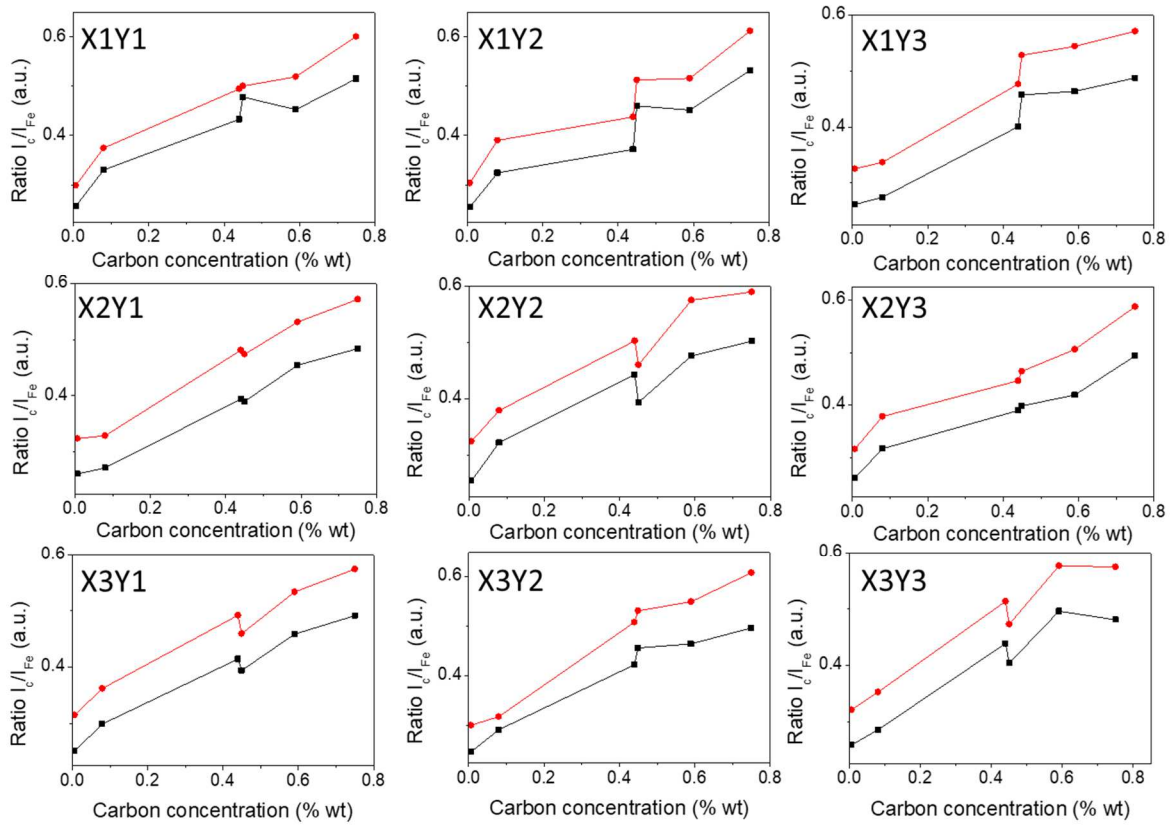

Figure 12 C I to Fe II lines ratio as a function of carbon content from micro-analysis. The red series was performed six months after the black one.

4.2.2. Calibration curve for local quantitative analysis

A "representative" calibration curve was built from averaged spectra from 9 craters on each sample. As the pollution is always present on the same samples, the layer of the first twenty laser shots should be removed before building the calibration curve. The coefficient of determination of the calibration curve (R^2) is 0.9910 after linear regression of the ratio of carbon and iron line intensities averaged over 230 laser shots from all 9 craters, as shown in Figure 13a.

The same procedure was then performed to find an executable calibration with a minimally destructive volume as described in the previous section. The coefficients of determination of all the attempted calibration curves for micro-analysis are shown in Figure 13b. It shows that the results of taking more than 50 spectra are similar after deleting more than the first twenty spectra. To analyze as little material as possible, we also built the final calibration curve with the 50 spectra (from the 21st to 70th laser shots) as in the macro-analysis and acquired an R^2 of 0.988, as shown in Figure 13c.

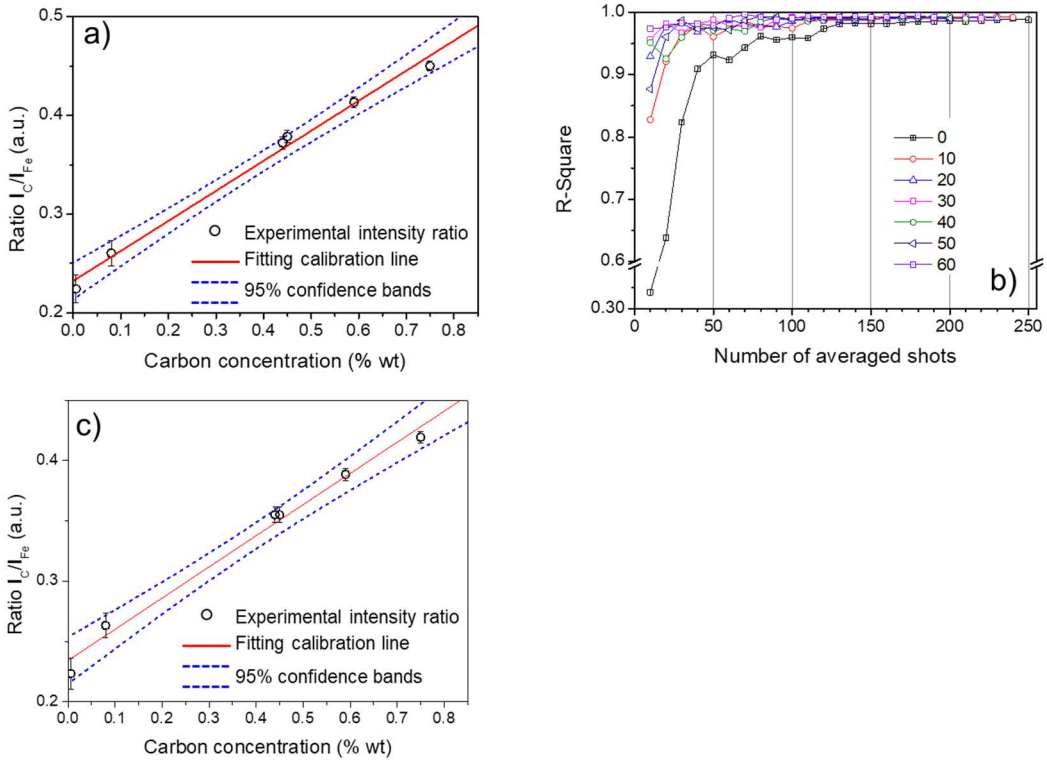

Figure 13 Micro-analysis calibration curve from the intensity ratio of carbon and iron line by averaged 230 spectra (**a**) and 50 spectra (**c**). **b**) Coefficients of determination (R^2) for all calibration curves after deleting the indicated number (0-60) of spectra from the surface.

The number of laser shots for each analyzed point can be reduced to 70, and therefore the duration of an experiment to scan a large surface can be reduced considerably without degrading the quantitative precision.

4.3. Influence of LIBS implementation on the macro- and micro-calibration

4.3.1. Evaluation of the quantitation of laser spot size

In the previous sections, the calibration curves were established by two modes of measurement with different spatial resolutions. We evaluated the limit of quantitation (LoQ) in order to estimate the lowest concentration from which these calibrations begin to provide reasonably reliable values. The LoQ of an individual analytical procedure is the lowest amount of analyte, the sampled material, which can be quantitatively determined with suitable precision and accuracy [29, 30]. LoQ allows us to assess and validate our LIBS implementation protocols. One method of obtaining the LoQ value is based on the calibration graph. The macro-analysis and micro-analysis calibration curves from 50 averaged spectra in Figures 11c and 13c are therefore plotted again in Figure 14 with their 95% prediction band. According to Mocak et al.[31], LoQ is the horizontal intersection of the intercept of the upper

limit of the prediction band with the lower limit of the prediction band. We thus got the LoQ value for macro-analysis (0.162 wt%) and that for micro-analysis (0.121 wt%).

As confirmed by statistics, the more spectra used to build the calibration curve, the more accurate the result will be [29]. The predicted band in the linear regression is thinner for micro-analysis because the macro-analysis has averaged 50 spectra whereas the micro-analysis has the same number of spectra, but at each of its 9 measurement locations. The slope of the linear regression equation reflects the sensitivity of quantitation. Thus, the macro-scale measurement is more sensitive than the micro-scale measurement. Broadly speaking, the macro-analysis is better for obtaining a global concentration, with a good ability to perform a quantitative analysis in terms of sensitivity and precision.

However, in practice, the accuracy, the analyzed material quantity, and the exam duration need balance. Fortunately, performing 70 laser shots is sufficient to measure the carbon content and to cover the carbon concentration range in steel.

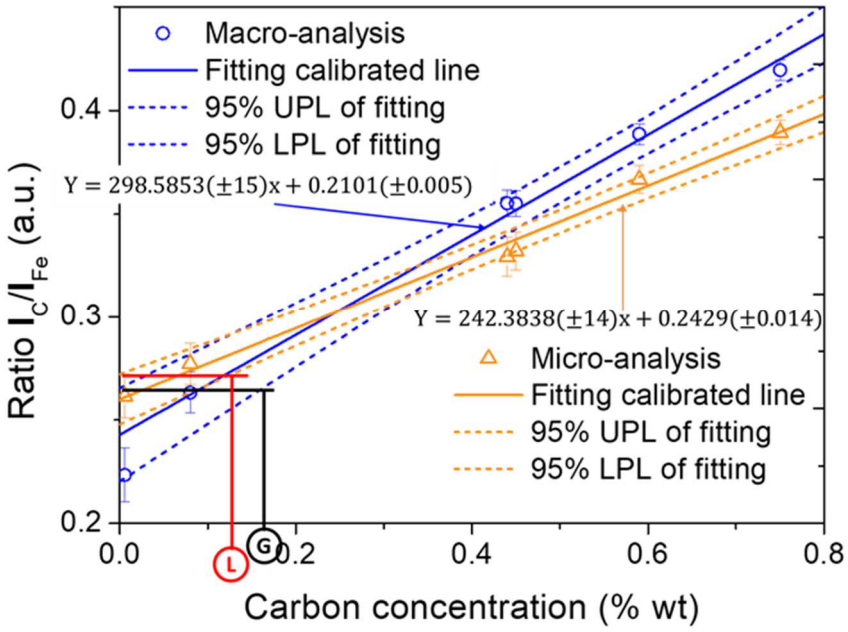

Figure 14 Calibration curves from 50 averaged spectra are present with their 95% prediction bands between the dotted line for each mode of measurement. UPL: upper predicted limits; LPL: lower predicted limits; **G**: LoQ of macro-analysis, **L**: LoQ of micro-analysis.

The two calibration curves in Figure 14 are different in terms of slope and origin. This highlights the difficulty of working with plasmas generated in different conditions of laser-material interaction. The influence of the sampled volume at each shot can change the global species density in the plasma. Additionally, even by looking for the "same" plasma condition for the measurement in terms of plasma temperature and electron density conditions, the

optimization of the signal-to-noise ratio induces a difference in the signal collected in the state of the plasma scanned. It is then necessary to use the proper calibration curve to ensure an accurate measurement.

4.3.2. Evaluation of the influence of laser ablation environment

A key element in building calibration curves is obtainment of a reliable ratio of carbon to iron line emission intensities. The plasma is a temporal light source, and the characteristics of plasma emission depend on its temporal and spatial evolution and environment [25, 32-34].

It should be noted that the same fluence for different laser spot sizes means that the total laser energy deposited in these two systems is different. For macro-analysis, the quantity of ablated material for one laser shot is greater than for micro-analysis. Consequently, electron density in the plasma and the temperature are both higher. The interaction between the plasma and ambient gas allows the exchange of energy between them. Thus, in the gas mixture, more He is needed to reduce the electron density, and the detection delay is longer to cool the plasma down until the carbon emission line is optimized. By contrast, in micro-analysis, the life duration of the plasma is shorter, and more Ar is needed to maintain the electron density and the temperature. Hence, the detection delay is reduced to reach the condition of a hot plasma.

In our observed spectral range, the upper energy level of Fe II lines varies from 7.695 eV (Fe II 205.733 nm) to 9.1711eV (Fe II 188.10 nm), and almost no Fe atom line is found. The Fe ion lines are not the resonant ones, so the approximation for optically thin lines can be applied in this case, although the iron is the abundant element in the steel sample. The plasma induced from a steel sample in argon during the detection delay could be considered to be a uniform plasma in local thermodynamic equilibrium (LTE) state [35]. The plasma temperature was thus estimated by a Boltzmann plot for each measurement from the Fe ions lines [36].

Figure 15 shows a Boltzmann plot obtained using the spatially integrated intensities of Fe lines from macro- (a) and micro- (b) analysis on sample No. 5. The temperature can be deduced by the slope of this linear fitting. However, due to the lack of a large enough upper level energy gap of the transition in our detection spectral range, the estimation of the plasma temperature has about 50% uncertainty.

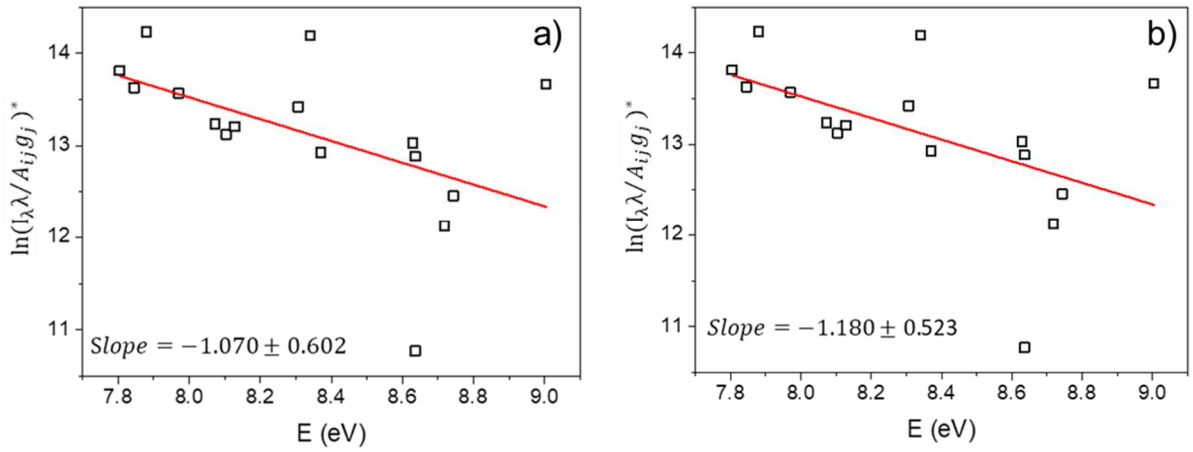

Figure 15 Boltzmann plot obtained using the spatially-integrated intensities of Fe lines from macro- (a) and micro- (b) analysis on sample No. 5.

The plasma temperatures from the 6 samples were calculated separately, and the mean values were 10674±731 K for micro-analysis and 10269±293 K for macro-analysis. All these plasmas were at the same temperature after adjusting the detection time window and conditioning of the gas environment. This temperature offers a detectable carbon emission with a good signal-to-noise ratio. Thus, we assume that an ideal plasma exists in terms of the optimization of quantitative analysis, and these results encourage us to perform future research about it.

4.4. Quantitative analysis of archaeological pieces

The evaluation of the impact of LIBS implementation on the macro- and micro-calibration allows the quantitative analysis to be performed on steel samples with good precision. In this work, our archaeological sample has a thickness of about 5 mm, and the resolution of phase distribution of this archaeological piece is inferior to 220 µm (Figure 3b). A micro-analysis (50 µm) is hence more suitable.

A linear scanning of the surface of that cross section was carried out with a 100-µm interval between two analyzed points. The same experimental parameters and protocol were applied as the previous micro-analysis on reference samples. A number of 250 laser shots were performed on one position, and the intensity ratios of C I and Fe II lines were calculated by averaging all remaining 230 spectra and by averaging 50 spectra after deleting the first 20. The ratios were then computed from the respective calibration curves. We plot the carbon concentration as a function of analyzed positions in Figure 16a. We obtained a similar carbon concentration for the same position by using these two calibration curves built by 230 and 50

spectra for micro-analysis. It shows that using a mean of 50 spectra did not change the figure of merit of the quantitative analysis, and thus allows us to reduce experimental duration.

The carbon concentration deduced by averaging 50 spectra is put on the microscopic image where the analysis was performed (Figure 16b). The same carbon concentration was obtained from the metallographic observation.

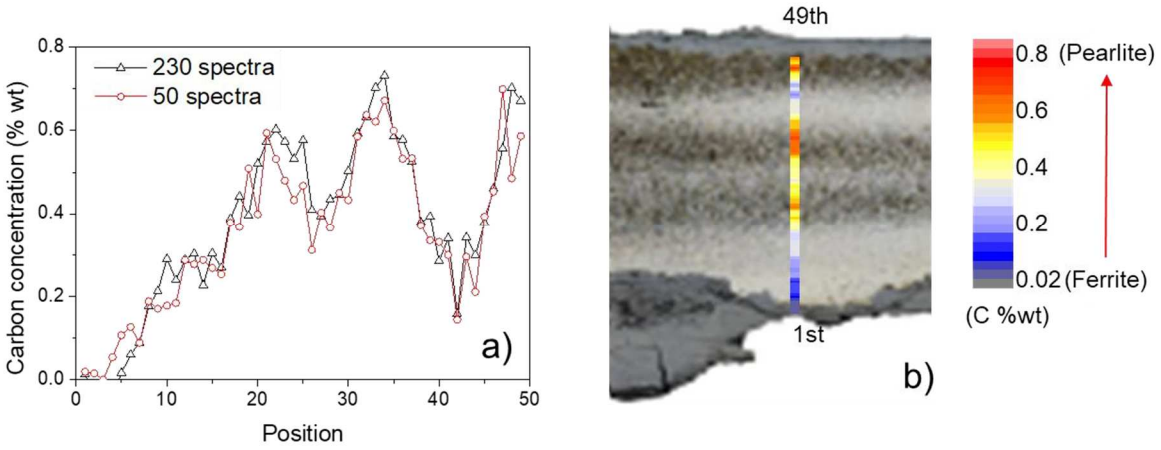

Figure 16 a) carbon concentration on archaeological piece from micro-analysis **b**) The micro-analysis carbon concentration (as well the steel phase) superposed on the microscopic image.

As we know, the pure pearlite phase contains 0.8 wt% carbon content, and the ferrite phase has at maximum 0.02 wt%. The carbon content in ferrite is below the LoQ and close to the limit of detection, but the C emission was still detected. According to the distribution of carbon content, the steel phase distribution can be deduced. Moreover, quantitative metallography is possible only in case the structure formed after slow cooling. This is not the case for the majority of artefacts. Thus, LIBS provides a reliable, alternative, and rapid means of analyzing archaeological pieces compared to the quantitative metallography approach.

5. Conclusion

In this work, we demonstrated that, unlike traditional analytical techniques, LIBS can be used to conduct a stratigraphic examination on solid material. It can also help to remove surface pollution and to obtain a more accurate result, especially when the pollution layer contains the targeted element.

LIBS analytical technique provides the advantage of its high level of sensitivity to characterize solid materials, in particular for light elements at low concentration. Besides detecting low carbon content, one supplementary challenge to perform LIBS analysis on steel

is that strong and abundant iron emission lines produce an interference with the carbon line present in the same spectral detection window. A carbon emission line at 193.09 nm is a good choice for low carbon concentration steel analysis, but a high-resolution spectrometer is necessary in order to avoid this interference.

The experimental parameters and measurement protocols are decisive factors to LIBS analysis quality. Two types of measurements were used, namely macro- and micro- analyses, which were defined by the relationship between the size of the laser beam and the inhomogeneity of the carbon spatial distribution. We obtained a similar nature of plasma induced by two sizes of laser spots in two specially prepared gas environments. The implementation of these two protocols provided the same level of ability to quantify the carbon content in the steel.

This work achieved the identification of different steel phases of an archaeological sample. This result provides a strategy that leads to a new path for future measurements on samples for which the metallographic approach is not possible (fast cooled or quenched steels). Moreover, it can also be employed with minimum sample preparation and applied directly on the artefact, without any sampling. This could be possible on objects with very little surface corrosion, such as certain armor or weapons in collections of museums. This would take advantage of the quasi non-invasive nature of LIBS, whose execution only generates almost invisible craters.

Acknowledgements

This work has been supported by the French Ministry Research Program EquipEx PATRIMEX ANR-11-EQPX-0034 and the DIM MAP of the Ile de France Region.

Thanks to Rémi Petitcol, Ruven Pillay from the C2RMF for carefully editing the manuscript.

Reference

1 M.F. Ashby, D.R.H. Jones, Engineering materials: An introduction to their properties and applications, in, Pergamon press, Oxford, 1996.

2 ASM Handbook: Mechanical testing and evaluation, in, ASM International, 2000.

3 S. Leroy, M. Hendrickson, S. Bauvais, E. Vega, T. Blanchet, A. Disser, E. Delque-Kolic, The ties that bind: archaeometallurgical typology of architectural crampons as a method for reconstructing the iron economy of Angkor, Cambodia (tenth to thirteenth c.), Archaeological and Anthropological Sciences, 10 (2018) 2137-2157.

4 R. Pleiner, Iron in archaeology: the European bloomery smelters, Archeologický ústav AVČR, 2000.

5 G. Pagès, P. Dillmann, P. Fluzin, L. Long, A study of the Roman iron bars of Saintes-Mariesde-la-Mer (Bouches-du-Rhône, France). A proposal for a comprehensive metallographic approach, Journal of Archaeological Science, 38 (2011) 1234-1252.

6 J.-B. Seol, B.-H. Lee, P. Choi, S.-G. Lee, C.-G. Park, Combined nano-SIMS/AFM/EBSD analysis and atom probe tomography, of carbon distribution in austenite/ε-martensite highMn steels, Ultramicroscopy, 132 (2013) 248-257.

7 G.F. Vander Voort, S.R. Lampman, B.R. Sanders, G.J. Anton, C. Polakowski, J. Kinson, K. Muldoon, S.D. Henry, W.W. Scott Jr, ASM handbook, Metallography and microstructures, 9 (2004) 44073-40002.

8 M.A. Khater, Low Level Carbon Detection in Steel Alloys Based on Optimization of Observation Conditions of Laser-Induced Breakdown Spectroscopy (LIBS) in Ambient Air, World Journal of Applied Physics, 1 (2016) 16.

9 T.A. Labutin, S.M. Zaytsev, A.M. Popov, N.B. Zorov, Carbon determination in carbonmanganese steels under atmospheric conditions by Laser-Induced Breakdown Spectroscopy, Optics express, 22 (2014) 22382-22387.

10 L. Dudragne, P. Adam, J. Amouroux, Time-resolved laser-induced breakdown spectroscopy:
application for qualitative and quantitative detection of fluorine, chlorine, sulfur, and carbon in air, Applied Spectroscopy, 52 (1998) 1321-1327.

11 R. Noll, C. Fricke-Begemann, S. Connemann, C. Meinhardt, V. Sturm, LIBS analyses for industrial applications–an overview of developments from 2014 to 2018, Journal of Analytical Atomic Spectrometry, 33 (2018) 945-956.

12 R. Noll, V. Sturm, Ü. Aydin, D. Eilers, C. Gehlen, M. Höhne, A. Lamott, J. Makowe, J. Vrenegor, Laser-induced breakdown spectroscopy—from research to industry, new frontiers for process control, Spectrochimica Acta Part B: Atomic Spectroscopy, 63 (2008) 1159-1166.

13 M.A. Khater, Laser-induced breakdown spectroscopy for light elements detection in steel: State of the art, Spectrochimica Acta Part B: Atomic Spectroscopy, 81 (2013) 1-10.

14 L. Zhang, W. Ma, L. Dong, X. Yan, Z. Hu, Z. Li, Y. Zhang, L. Wang, W. Yin, S. Jia, Development of an apparatus for on-line analysis of unburned carbon in fly ash using laserinduced breakdown spectroscopy (LIBS), Applied spectroscopy, 65 (2011) 790-796.

15 V. Detalle, Analyse de l'homogénéité du combustible nucléaire MOX par Spectrométrie d'Emission optique sur Plasma Induit par Laser (SEPIL), in, Lyon 1, 1999.

16 V. Sturm, J. Vrenegor, R. Noll, M. Hemmerlin, Bulk analysis of steel samples with surface scale layers by enhanced laser ablation and LIBS analysis of C, P, S, Al, Cr, Cu, Mn and Mo, Journal of analytical atomic spectrometry, 19 (2004) 451-456.

17 E. Tognoni, V. Palleschi, M. Corsi, G. Cristoforetti, Quantitative micro-analysis by laserinduced breakdown spectroscopy: a review of the experimental approaches, Spectrochimica Acta Part B: Atomic Spectroscopy, 57 (2002) 1115-1130.

18 M.S. Afgan, Z. Hou, Z. Wang, Quantitative analysis of common elements in steel using a handheld μ-LIBS instrument, Journal of Analytical Atomic Spectrometry, 32 (2017) 19051915.

19 L. Peter, V. Sturm, R. Noll, R. Hakala, J. Viirret, B. Overkamp, P. Koke, Multielemental analysis of low-alloyed steel by laser-induced breakdown spectrometry, in: Laser Metrology and Inspection, International Society for Optics and Photonics, 1999, pp. 256265.

20 P. Dillmann, F. Téreygeol, C. Verna, Premières analyses métallographiques des produits sidérurgiques trouvés sur le site médiéval de Castel-Minier (Aulus-les-Bains, 09), ArcheoSciences. Revue d'archéométrie, (2006) 7-14.

21 F. Téreygeol, Le Castel-Minier (Aulus-les-Bains), rapport intermédiaire, in, DRAC MidiPyrénées, 2016.

22 J. Aguilera, C. Aragon, J. Campos, Determination of carbon content in steel using laserinduced breakdown spectroscopy, Applied spectroscopy, 46 (1992) 1382-1387.

23 J. Aguilera, C. Aragon, A comparison of the temperatures and electron densities of laserproduced plasmas obtained in air, argon, and helium at atmospheric pressure, Applied Physics A, 69 (1999) S475-S478.

24 R. Bruder, Etude et développement de la spectroscopie d'émission optique sur plasma induit par laser pour l'analyse de terrain: un exemple d'application aux œuvres d'art, in, Paris 6, 2008.

25 X. Bai, A. Pin, J. Lin, M. Lopez, C.K. Dandolo, P. Richardin, V. Detalle, The first evaluation of diagenesis rate of ancient bones by laser-induced breakdown spectroscopy in archaeological context prior to radiocarbon dating, Spectrochimica Acta Part B: Atomic Spectroscopy, 158 (2019) 105606.

26 C. Pan, X. Du, N. An, Q. Zeng, S. Wang, Q. Wang, Quantitative analysis of carbon steel with multi-line internal standard calibration method using laser-induced breakdown spectroscopy, Applied spectroscopy, 70 (2016) 702-708.

27 N.B. Zorov, A.A. Gorbatenko, T.A. Labutin, A.M. Popov, A review of normalization techniques in analytical atomic spectrometry with laser sampling: From single to multivariate correction, Spectrochimica Acta Part B: Atomic Spectroscopy, 65 (2010) 642657.

28 NIST Atomic Spectra Database: https://www.nist.gov/pml/atomic-spectra-database.

29 J.-M. Mermet, Limit of quantitation in atomic spectrometry: An unambiguous concept?, Spectrochimica Acta Part B: Atomic Spectroscopy, 63 (2008) 166-182.

30 J.-M. Mermet, Calibration in atomic spectrometry: A tutorial review dealing with quality criteria, weighting procedures and possible curvatures, Spectrochimica Acta Part B: Atomic Spectroscopy, 65 (2010) 509-523.

31 J. Mocak, A.M. Bond, S. Mitchell, G. Scollary, A statistical overview of standard (IUPAC and ACS) and new procedures for determining the limits of detection and quantification: application to voltammetric and stripping techniques (technical report), Pure and Applied Chemistry, 69 (1997) 297-328.

32 X. Bai, Q. Ma, V. Motto-Ros, J. Yu, D. Sabourdy, L. Nguyen, A. Jalocha, Convoluted effect of laser fluence and pulse duration on the property of a nanosecond laser-induced plasma into an argon ambient gas at the atmospheric pressure, Journal of applied physics, 113 (2013) 013304.

33 J. Yu, Q. Ma, V. Motto-Ros, W. Lei, X. Wang, X. Bai, Generation and expansion of laserinduced plasma as a spectroscopic emission source, Frontiers of Physics, 7 (2012) 649-669.

34 A. Löbe, J. Vrenegor, R. Fleige, V. Sturm, R. Noll, Laser-induced ablation of a steel sample in different ambient gases by use of collinear multiple laser pulses, Analytical and bioanalytical chemistry, 385 (2006) 326-332.

35 J. Hermann, D. Grojo, E. Axente, C. Gerhard, M. Burger, V. Craciun, Ideal radiation source for plasma spectroscopy generated by laser ablation, Physical Review E, 96 (2017) 053210.

36 J. Aguilera, C. Aragón, Multi-element Saha–Boltzmann and Boltzmann plots in laserinduced plasmas, Spectrochimica Acta Part B: Atomic Spectroscopy, 62 (2007) 378-385.

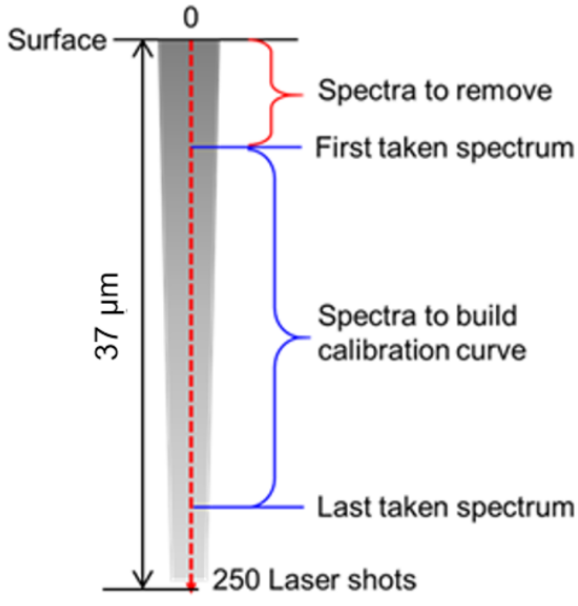
0
Surface
Spectra to remove
First taken spectrum
37 µm
Spectra to build
calibration curve
Last taken spectrum
250 Laser shots

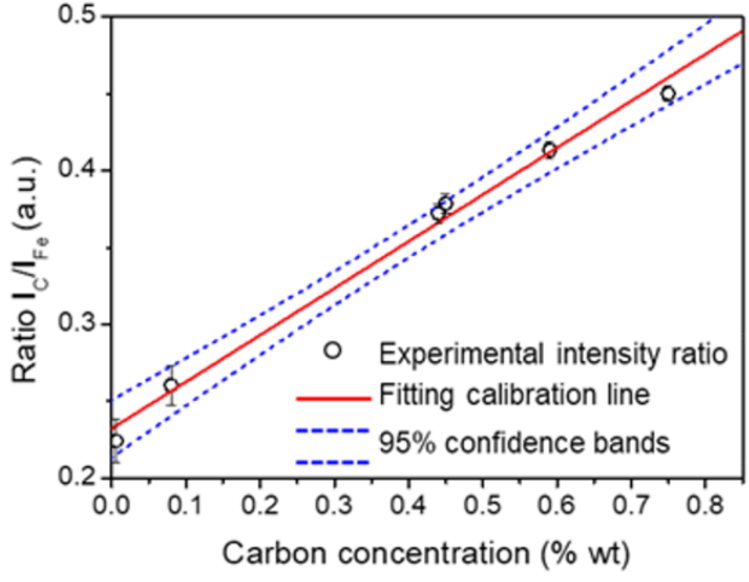
0.5
0.4
0.3
0.2
Ratio I_C/I_{Fe} (a.u.)
0.0
0.1
0.2
0.3
0.4
0.5
0.6
0.7
0.8
Carbon concentration (% wt)
Experimental intensity ratio
Fitting calibration line
95% confidence bands

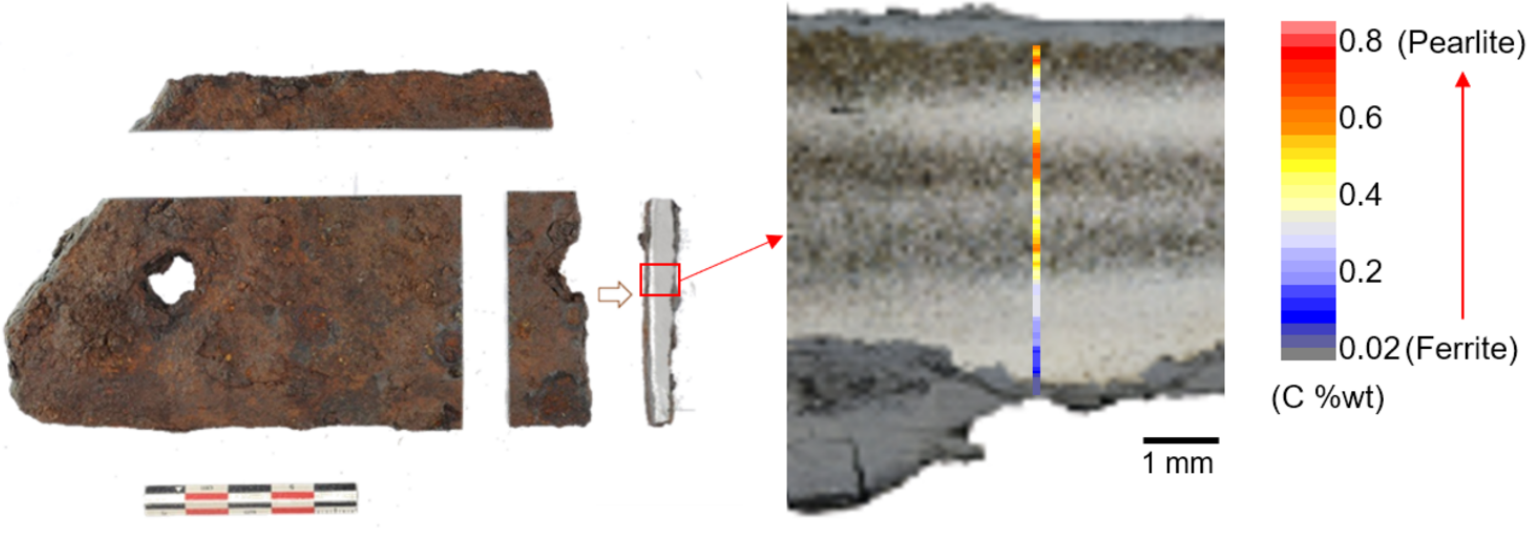
0.8 (Pearlite)
0.6
0.4
0.2
0.02 (Ferrite)
(C %wt)
1 mm